The beneficial role of nano-sized Fe3O4 entrapped in ultra-stable Y zeolite for the complete mineralization of phenol by heterogeneous photo-Fenton under solar light

Chemosphere 345 (2023) 140400

Contents lists available at ScienceDirect

Chemosphere

journal homepage: www.elsevier.com/locate/chemosphere

The beneficial role of nano-sized Fe_3O_4 entrapped in ultra-stable Y zeolite for the complete mineralization of phenol by heterogeneous photo-Fenton under solar light

Olimpia Tammaro [a,1], Nicola Morante [b,1], Antonello Marocco [c], Marco Fontana [a,d], Micaela Castellino [a], Gabriele Barrera [e], Paolo Allia [a,e], Paola Tiberto [e], Rossella Arletti [f], Riccardo Fantini [f], Vincenzo Vaiano [b], Serena Esposito [a,*], Diana Sannino [b,**], Michele Pansini [c]

[a] Department of Applied Science and Technology and INSTM Unit of Torino – Politecnico, Politecnico di Torino, Corso Duca degli Abruzzi 24, 10129, Torino, Italy
[b] Department of Industrial Engineering, University of Salerno, Via Giovanni Paolo II, 132, 84084, Fisciano, SA, Italy
[c] Department of Civil and Mechanical Engineering and INSTM Research Unit, Università degli Studi di Cassino e del Lazio Meridionale, Via G. Di Biasio 43, Cassino, FR 03043, Italy
[d] Center for Sustainable Future Technologies @POLITO, Istituto Italiano di Tecnologia, Via Livorno 60, Turin, 10144, Italy
[e] INRiM Torino, Advanced Materials for Metrology and Life Sciences, Strada delle Cacce 91, 10143, Torino, Italy
[f] Università degli Studi di Modena e Reggio Emilia, Chemical and Geological Sciences, Via Campi 103, Modena, 41125, Italy

HIGHLIGHTS

- Stable catalysts were prepared by entrapping Fe species in ultra-stable Y zeolite.
- The catalyst's magnetic properties allow easy separation and reuse.
- Complete phenol removal is achieved by solar light-driven photo-Fenton reaction.
- Phenol mineralization increases with Fe_3O_4 content in ultra-stable Y zeolite.
- Hydroxyl radicals play the main role in the removal of phenol under solar light.

GRAPHICAL ABSTRACT

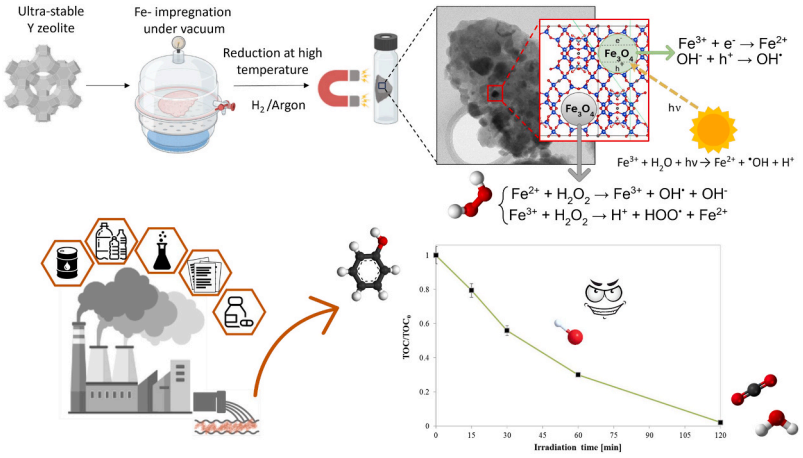

ARTICLE INFO

Handling Editor: S Garcia-Segura

ABSTRACT

Highly efficient, separable, and stable magnetic iron-based-photocatalysts produced from ultra-stable Y (USY) zeolite were applied, for the first time, to the photo-Fenton removal of phenol under solar light. USY Zeolite with

* Corresponding author.
** Corresponding author.
E-mail addresses: serena_esposito@polito.it (S. Esposito), dsannino@unisa.it (D. Sannino).
[1] The authors Olimpia Tammaro and Nicola Morante contributed equally.

https://doi.org/10.1016/j.chemosphere.2023.140400
Received 9 August 2023; Received in revised form 26 September 2023; Accepted 8 October 2023
Available online 18 October 2023

Keywords:
Ultrastable Y zeolites
Nano-sized Fe_3O_4
Magnetic catalyst
Phenol
Photo-fenton
Solar light

a Si/Al molar ratio of 385 was impregnated under vacuum with an aqueous solution of Fe^{2+} ions and thermally treated (500–750 °C) in a reducing atmosphere. Three catalysts, Fe-USY500°C-2h, Fe-USY600°C-2h and Fe-USY750°C-2h, containing different amounts of reduced iron species entrapped in the zeolitic matrix, were obtained. The catalysts were thoroughly characterized by absorption spectrometry, X-ray powder diffraction with synchrotron source, followed by Rietveld analysis, X-ray photoelectron spectroscopy, N_2 adsorption/desorption at −196 °C, high-resolution transmission electron microscopy and magnetic measurements at room temperature.

The catalytic activity was evaluated in a recirculating batch photoreactor irradiated by solar light with online analysis of evolved CO_2. Photo-Fenton results showed that the catalyst obtained by thermal treatment at 500 °C for 2 h under a reducing atmosphere (FeUSY-500°C-2h) was able to completely mineralize phenol in 120 min of irradiation time at pH = 4 owing to the presence of a higher content of entrapped nano-sized magnetite particles. The latter promotes the generation of hydroxyl radicals in a more efficient way than the Fe-USY catalysts prepared at 600 and 750 °C because of the higher Fe_3O_4 content in ultra-stable Y zeolite treated at 500 °C. The FeUSY-500°C-2h catalyst was recovered from the treated water through magnetic separation and reused five times without any significant worsening of phenol mineralization performances. The characterization of the FeUSY-500°C-2h after the photo-Fenton process demonstrated that it was perfectly stable during the reaction. The optimized catalyst was also effective in the mineralization of phenol in tap water. Finally, a possible photo-Fenton mechanism for phenol mineralization was assessed based on experimental tests carried out in the presence of scavenger molecules, demonstrating that hydroxyl radicals play a major role.

1. Introduction

Phenol is classified as acutely toxic and is considered one of the most hazardous substances in surface and groundwater (Kulkarni and Kaware, 2013; Villegas et al., 2016). It is widely used in various sectors such as the petrochemical industry, the production of paints, the textile industry, pesticide synthesis plants, the food industry and the production of various types of resins (Saeed and Ilyas, 2013; Mancuso et al., 2022). Consequently, a significant amount of phenol is present in the wastewater disposed of by such industries (Kuši et al., 2006). The presence of phenol in water bodies is a source of serious forms of pollution as it is capable of inducing carcinogenic and mutagenic effects on human and aquatic life (Villegas et al., 2016; Babuponnusami and Muthukumar, 2011; U. EPA, 2002).

Moreover, phenol's high-water solubility and chemical stability make its removal by conventional biological wastewater treatment virtually impossible (Babuponnusami and Muthukumar, 2011). Therefore, it is necessary to develop alternative treatment technologies, such as wet air oxidation, catalytic wet air oxidation and advanced oxidation processes (AOPs), to be used either individually or in combination (Suarez-Ojeda et al., 2008; Quintanilla et al., 2010). Among these methods, AOPs (such as Fenton and photo-Fenton processes) represent valid methods for the in-situ remediation of water and wastewater in mild conditions (Bahadori et al., 2018). The Fenton and photo-Fenton processes can oxidize phenol to CO_2 and water, thanks to the generation of hydroxyl radicals ($HO^{\bullet}$) and other minor reactive oxygen species at ambient temperature and pressure. In particular, the Fenton process uses Fe^{2+} ions and hydrogen peroxide (H_2O_2) to convert Fe^{2+} ions into Fe^{3+} ions, producing hydroxyl radicals. To regenerate Fe^{2+} ions (necessary for the generation of hydroxyls radical), the reduction of Fe^{3+} into Fe^{2+} occurs simultaneously in the reaction system thanks to the reaction of Fe^{3+} with H_2O_2, producing $HO_2^{\bullet}$. However, this reduction step is slow (Kwan and Voelker, 2003). To overcome this drawback, it was found that UV irradiation gives rise to Fe^{3+} reduction, yielding further hydroxyl radicals, and enhancing the degradation performances (photo-Fenton process) (Oancea and Meltzer, 2013).

Despite their high potential, the Fenton and photo-Fenton methods based on homogeneous Fe ions suffer from several disadvantages, such as the limited pH range of operation, the production of sludge due to Fe-precipitate, and the need to remove the homogeneous catalyst after oxidation to prevent the Fe content from exceeding standard discharge limits (Segneanu et al., 2013; Elshorbagy and Chowdhury, 2013). To overcome these limitations, scientific research is increasingly focusing on preparing and fine-tuning heterogeneous catalysts for Fenton and photo-Fenton processes.

Among the tested materials, $LaFeO_3$ and $Pt/LaFeO_3$ perovskites loaded onto cordierite or corundum honeycomb monoliths were found to be effective in the photo-Fenton removal of several water pollutants under UVC irradiation (Sannino et al., 2011, 2012; Vaiano et al., 2014, 2015). Moreover, nanomaterials such as imogolite-related materials modified with iron were successfully applied as heterogeneous catalysts in the photo-Fenton removal of tartrazine dye in the presence of UV-A light (Bahadori et al., 2018). Suitably modified zeolites were also tested in the heterogeneous Fenton and photo-Fenton processes under UV light. It was shown that these materials are able to host iron (III) species in the zeolite framework in a very effective way. Their activity in Fenton processes was demonstrated in (Noorjahan et al., 2005), where Fe(III)-HY catalysts (Si/Al∼2.6; specific surface area (SSA) = 500 m^2g^{-1}) were prepared and tested for photo-assisted Fenton oxidation of phenol. In particular, the influence on the photo-Fenton activity of Fe (III) ions loaded by an impregnation method was studied under UVC irradiation. More recently, Ayoub et al. reported that zeolite-based Fenton catalysts can degrade micro-pollutants with an efficiency comparable to that achieved in the homogeneous Fenton reaction (Ayoub et al., 2018). In particular, the faujasite Y zeolite, impregnated with iron (III) at 20 wt% showed complete photo-Fenton removal of phenol (10 ppm) under UV light within 60 min, although the authors report neither stability nor activity studies in the visible region. Furthermore, iron leaching is significantly high, reaching 4 ppm in the treated water. Fe/HY zeolite has been also applied for photo-Fenton degradation of polyvinyl alcohol (Bossmann et al., 2001).

Recently, magnetite (Fe_3O_4) and magnetite based-catalysts received great attention both as a heterogeneous Fenton and photo–Fenton catalyst because of their low cost, the possibility of magnetic separation, nontoxicity, and good stability (Liu et al., 2021; Huang et al., 2022). Fe_3O_4 possesses an inverse spinel structure, $(Fe^{3+})_A(Fe^{2+}Fe^{3+})_BO_4$ where A and B represent tetrahedral and octahedral atom positions, respectively (Abadiah et al., 2019). Phenol can be removed by magnetite micrometric and nanometric particles where the high specific surface area possesses a relevant role in sorption and/or redox processes. However, their strong aggregation in neutral or acidic solutions, as the main drawback, must be prevented (Minella et al., 2014). As a result, different types of Fe_3O_4-based systems have been studied, often in elaborate catalytic formulations (Zhong et al., 2021; Gong et al., 2019).

Although significant progress has been made so far in photo-Fenton processes, the real challenge remains to exploit sunlight instead of UV light with catalytic formulations requiring simple and industrially scalable syntheses, thus making photo-activated processes efficient, sustainable and economical (Konstantinou and Albanis, 2004).

Based on all the previous considerations, the experience acquired by some of us in the production of tailored nanostructured metal-ceramic materials from zeolite precursors (Marocco et al., 2012; Pansini et al.,

2017, 2018; Freyria et al., 2019; Manzoli et al., 2021; Sannino et al., 2022; Esposito et al., 2018; Tammaro et al., 2023) has driven research toward the conscious development of zeolite-based catalysts for Fenton and photo-Fenton reaction.

In particular, the ultra-stable Y zeolite (USY) in its hydrogen form was selected for its high thermal stability to retain the zeolite porous architecture, crucial for the catalytic application. USY zeolite is well-known from the sixties of the past century and its use is widespread as a catalyst for the cracking reaction of high molecular weight hydrocarbons, residual of the topping operations of oil (Liu et al., 2022). Its synthesis and dealumination procedure has been optimized for a long time, which results in its low cost (Breck and Smith, 1959; Neamţ et al., 2004a). Other reasons that strongly supported this choice are as follows.

1. Its high Si/Al ratio makes USY zeolite highly hydrophobic. This feature favors the transfer of scarcely polar organic compounds (such as many organic pollutants present in waters) from the water phase to the catalyst phase, thus making easier the first step of their catalytic oxidation (Breck and Smith, 1959; Neamţ et al., 2004a).
2. USY zeolite exhibits a tridimensional system of micropores (opening of about 9 Å) and a certain amount of large mesopores generated by the post-synthesis dealumination procedure, that may favor the formation of embedded nanoparticles within the structure. Moreover, among the high-silicon zeolites, the USY zeolite stands out for its outstanding specific surface area (the order of hundreds of square meters per gram) as well as its large external surface area (Morales et al., 2020).

About the use of ultra-stable zeolites for environmental applications, there are few works reported in the literature. Santos et al. studied only the degradation of azo dyes by the heterogeneous Fenton process by comparing the activity of ion-exchanged Fe–Y and Fe-USY (Si/Al ratio of 4.5) zeolites (Santos et al., 2020). However, it must be considered that only oxidized iron species are present in both Y and USY zeolites.

Moreover, a USY zeolite with a SiO_2/Al_2O_3 molar ratio of 11.5, exchanged with Fe(III) (at 1.69 wt% of iron) was applied for the catalytic wet peroxide oxidation of reactive azo dyes by Neamţu et al. (Neamţ et al., 2004b). Despite the interesting reported results, it is worthwhile to note that the catalytic wet peroxide oxidation by using iron-based catalysts suffers from metal leaching and deactivation phenomena, as reported in the literature (Rueda Má et al., 2018).

Surprisingly, to date and to the best of our knowledge, USY zeolite (highly dealuminated 390 HUA, $SiO_2/Al_2O_3 = 770$ M ratio) was never used as support for iron species active in Fenton or photo-Fenton oxidation of phenol or other organic pollutants present in water (Zhang et al., 2022). However, Fe cannot be massively introduced in the framework of the here-selected USY zeolite by cation exchange owing to its very poor cation exchange capacity, arising from its very high Si/Al ratio. To avoid this drawback, USY zeolite was Fe-impregnated. In particular, a specific procedure of impregnation of USY zeolite under reduced pressure, allowing high Fe loadings, was specially set up for this work. Finally, the materials obtained according to the impregnation procedure were subjected to thermal treatment under a reducing atmosphere at different temperatures, to obtain a different Fe_3O_4 content and study its role as a catalyst in the photo-Fenton oxidation of phenol under solar light. The formation of iron-containing magnetic phases provides an additional advantage to the catalyst, as it allows its easy separation from the reaction medium and contributes to the realization of an efficient process (Zhong et al., 2021; Gong et al., 2019). The catalysts were fully characterized from the structural, compositional, textural and magnetic points of view. After an initial screening to individuate the most performing photocatalyst, operating conditions were varied, in terms of hydrogen peroxide dosage, pH, comparison with the homogenous photoreaction and stability up to five cycles. In addition, the removal of phenol in tap water was verified. The characterization was repeated on the magnetically recovered best-performing catalyst to ascertain its stability in the reaction environment.

2. Materials and methods

2.1. Materials

Tosoh Corporation ultrastable Y zeolite HSZ-390HUA (Si/Al molar ratio = 385), hereafter simply named USY, was used as a base material in the preparation of catalysts. The standard solutions and solvents for the analytical determinations were all Carlo Erba HPLC grade. Salt $FeSO_4 \cdot 7H_2O$ (Aldrich, 99.5 wt %) and doubly distilled water Carlo Erba reagent grade were used in the preparation of the impregnating solution. The H_2/Ar gas mixture (H_2 3% volume), used to create the reducing atmosphere during the thermal treatments (4MS023BB product code), was supplied by Nippon Gases.

For the experimental test phenol (C_6H_5OH, 99%, Carlo Erba), hydrogen peroxide solution (H_2O_2, 30% (w/w) in H_2O, Sigma Aldrich), hydrochloric acid solution (HCl, 37% (w/w) in H_2O, Carlo Erba) were purchased and used as received; while the aqueous solutions were prepared by using water of Milli-Q purity (TOC <2 ppb, resistivity ≥18.2 mΩ cm).

Furthermore, the Hanna Instruments Iron CTK kit was used to evaluate the leaching of total iron in solution after the tests by colorimetric analysis.

2.2. Preparation of the impregnating solution

A saturated solution of ferrous sulphate heptahydrate, (solubility S ≈ 400 g L^{-1} at 25 °C) was used to impregnate the USY zeolite. It was prepared as follows. $FeSO_4 \cdot 7H_2O$ (Aldrich, 99.5 wt %) was dissolved in doubly distilled water at ≈ 7 °C, under continuous stirring and bubbling with argon. These expedients were used to avoid Fe^{2+} oxidation to Fe^{3+} during the impregnation procedure (Weidenthaler et al., 2005).

2.3. Preparation of the Fe-USY zeolites

The USY zeolite (framework type FAU (Baerlocher et al., 2007)) was subjected to the following vacuum impregnation procedure. Specifically, 30 g of zeolite were deposited on the bottom of a glass desiccator with a diameter of about 18 cm, equipped with a sealed lid with a two-way stopcock. This apparatus allowed us to easily perform the following sequence of operations.

1) The air present in the desiccator and the porous structure of the USY zeolite, contained therein, was evacuated by a Carpanelli electric pump, model MM56P2, 0.15 kW, 3360 rpm.
2) After about 2 h of evacuation, the stopcock connected to the pump was closed and the pump was switched off. Subsequently, the desiccator was flooded with a saturated ferrous sulphate heptahydrate solution prepared immediately before the flooding step. This operation was performed while maintaining the vacuum condition by opening the second stopcock. The amount of such solution entered in the desiccator was sufficient to create a head of about 1 cm between the solid on the bottom and the free surface of the liquid.

The USY zeolite was left in contact with the saturated solution of ferrous sulphate heptahydrate for 48 h. Thereafter, the solvent was removed by evaporation at a constant temperature of 60 °C in an oven for about 3 days. The obtained powder was subjected to ball milling (with a single sphere) for 2 h. The material obtained according to the described impregnation procedure was labeled as Fe-USY zeolite.

For the preparation of the catalysts, a certain amount of Fe-USY zeolite was loaded in high-density Al_2O_3 vessels. Then, such vessels were put in an Al_2O_3 tubular furnace (length = 91 cm, diameter = 6.9 cm), heated (15 °C/min of heating rate) up to 500, 600 or 750 °C, and kept at these temperatures for 2 h under a reducing atmosphere created

by a flow a gaseous mixture H_2/Ar (H_2 3% volume). Then, the furnace was turned off and left to cool down at room temperature together with the materials contained therein. At the end of each thermal treatment, the black powders recovered from the furnace, the final product of the whole process, were stored in the air before the catalysis applications. From now on, we will refer to the three different types of materials obtained at 500, 600 and 750 °C with the "speaking acronyms" Fe-USY500°C-2h, Fe-USY600°C-2h and Fe-USY750°C- 2h, respectively. Samples Fe-USY500°C-2h and Fe-USY750°C- 2h after their use as a catalyst for the photo-Fenton oxidation of phenol in water were labeled as Fe-USY500°C-2h PF and Fe-USY750°C- 2h PF, respectively.

2.4. Characterization of materials

The Fe content of the Fe-USY impregnated zeolite was determined as follows. A weighed sample of the Fe-USY zeolite was dissolved in an aqueous solution of hydrofluoric and perchloric acid, and the Fe concentration of the solution was determined by spectrophotometry of atomic absorption (PerkinElmer Analyst 100).

USY and Fe-USY zeolites, Fe-USY500°C-2h, Fe-USY600°C-2h, Fe-USY750°C- 2h and Fe-USY500°C-2h PF samples were characterized through X-ray powder diffraction analysis. A preliminary XRPD characterization was performed in the laboratory, exploiting a Panalytical X'Pert PRO diffractometer equipped with a Cu Kα tube operating a 40 KV and 40 mA. Data were collected from 3 to 90° 2 theta on an X Celerator MPS detector with a counting time of 200 s per step (0.02° per step) (Shafia et al., 2015).

To avoid the well-known effect of Fe fluorescence observed when analyzing Fe-rich powders with Cu Kα radiation, for selected samples, detailed quantitative phase analysis (QPA) was carried out exploiting synchrotron light. The powder of each sample was carefully mixed with Al_2O_3 standard powder and packed in a 0.5 mm boron capillary. Data collection was performed at MCX beamline at Elettra Sincrotrone Trieste on a 4-circle Huber diffractometer equipped with a high-count rate fast scintillator detector preceded by a pair of slits with a vertical aperture of 200 and 300 μm with a fixed wavelength of 0.8263 Å. The pattern was collected by spinning the capillary under the beam in the 2theta range 2–40 with step size 0.02 and 1 s counting time. To obtain quantitative phase analyses the combined Rietveld-RIR method (Gualtieri et al., 1999) was exploited, and the data were fitted using the EXPGUI interface (Toby, 2001) GSAS package (Larson and Von Dreele, 1994). For the Rietveld refinement, the starting model of the USY framework was taken from Parise et al., 1984) (Parise et al., 1984) and then refined (Fig. SI1, SI2 and SI3).

N_2 adsorption/desorption isotherms at −196 °C were measured on samples previously outgassed at 200 °C for 3 h to remove water and other atmospheric contaminants (Micrometrics ASAP, 2020Plus). Due to the microporous character of zeolites, the Langmuir method was used to calculate the specific surface area but for easy comparison with literature, BET surface area was also reported; the total pore volume (V_p) was determined from the amount of desorption N_2 at P/P0 = 0.98, the micropore volume (V_{mp}) and the external surface area (S_{ext}) were determined according to the t-plot method (Sannino et al., 2013). The evaluation of pore size distribution was obtained by the Tarazona Non-local density functional theory (NL-DFT) model. Heat-treated samples were compared only with pristine zeolite since the presence of sulphates in the impregnated sample, Fe-USY, can be detrimental to the instrumentation during the temperature outgassing step.

The magnetization curve of Fe-USY500°C-2h was measured at room temperature by means of a VSM magnetometer operating in the 0–17 kOe range. The diamagnetic contribution from the zeolite scaffold and the sample holder, containing the nanocomposite, was subtracted from the raw data.

(Scanning) Transmission Electron Microscopy ((S)TEM) was carried out with a TALOS F200X microscope (Thermo Fisher) equipped with four Silicon drift detectors (SDD) for Energy Dispersive X-ray (EDX) spectroscopy. Concerning sample preparation, the catalyst in powder form was dispersed in isopropyl alcohol and subsequently deposited on a Cu holey carbon TEM grid by drop-casting. The analysis of TEM data was performed with the Thermo Scientific Velox software. The visualization of crystalline structures was obtained with Vesta software (Koner et al., 2020) using the crystalline structure provided in the Database of Zeolite Structures (Baerlocher et al., 2007).

X-Ray Photoelectron Spectroscopy (XPS) analysis has been carried out by means of a PHI 5000 Versaprobe (Physical Electronics, Chanhassen MN - USA) spectrometer, equipped with a monochromated Al k-alpha X-ray line (1486.6 eV), coupled to a double neutralization source, made up by e-beam and an Ar^+ sources, to overcome surface charging phenomena due to non-conductive samples. Survey and High Resolution (HR) scans have been acquired with 187 and 23 eV pass energy (PE) values, respectively. A 100 μm circle spot has been used to collect signals from the sample's surface. Raw data have been analyzed by means of Multipak v.9.7 dedicated software. Background signal, from HR spectra, has been subtracted by using the Shirley function. HR spectra have been referred to C1s peak at 284.8 eV, assigned to C–C in adventitious carbon.

A bar sample containing metal iron has been used as a reference for our zeolites experimental data acquired; Fe photoelectrons peaks have been acquired after 10 min Ar^+ sputtering at 2 kV accelerated voltage, to completely remove native oxide, to get a clear Fe^0 signal.

2.5. Photo-fenton activity tests

The tests were conducted in a cylindrical batch reactor (ID = 2.6 cm, L_{TOT} = 41 cm, and V_{TOT} = 200 mL) equipped with (i) a nitrogen distributor device (flow rate of 142 Ncc min^{-1}), (ii) a peristaltic pump (Watson Marlow) to maintain continuously recirculated the suspension avoiding the sedimentation of photocatalytic powder at the bottom of the reaction system, and (iii) four solar lamps (SUN-GLO, nominal power: 8 W each, irradiance: 24 mW cm^{-2}), placed around the external surface of the photoreactor at an equal distance from it (about 30 mm), to irradiate uniformly the volume of the solution, were used. In Fig. SI4 the schematic sketch of the experimental setup is shown.

The tests were conducted using 100 mL of an aqueous solution, with an initial concentration of phenol equal to 50 mg L^{-1}, a H_2O_2 dosage in the range 0.266–0.798 g L^{-1}, the first corresponding to the stoichiometric value to get the total oxidation of phenol, according to the reaction:

$$C_6H_5OH + 14\ H_2O_2 \rightarrow 17\ H_2O + 6\ CO_2 \quad \text{Eq (1)}$$

To assess whether and how the inorganic ion species affect the photodegradation process, tests were conducted by dissolving phenol in both distilled water and tap water. The properties of the selected tap water used for the test are listed in Table SI1.

The dosage of the photocatalyst was 3 g L^{-1}. This dosage was optimized in previous works in which the same photoreactor configuration was used (Vaiano et al., 2018, 2019).

Initially, the suspension containing phenol was placed in the reactor, and after it was closed, the nitrogen stream was fluxed at ambient temperature for 10 min. Subsequently, H_2O_2 was introduced into the system and lamps were turned on in order to initiate the reaction. After 60 min of testing, the same volume of H_2O_2 aqueous solution was injected into the reaction system.

Samples of the treated solution (3 mL) were collected for analyses at fixed times. The reaction products in the gas phase were monitored through continuous analyzers to measure the gaseous CO_2 concentration (Uras 14, ABB) at the reactor outlet. The reaction pressure was 1 atm. The Total Organic Carbon (TOC) was evaluated as a function of time based on the CO_2 concentrations recorded in the gaseous phase leaving the reactor. The H_2O_2 residual concentration in the solution was determined using a UV–Vis spectrophotometer (Lambda 35, PerkinElmer) by measuring the absorbance of the H_2O_2/$TiOSO_4$ complex at λ = 410 nm (Eisenberg, 1943).

3. Results and discussion

3.1. Chemical composition

The USY zeolite used in this work has a negligible cation exchange capacity due to the very high silicon/aluminum ratio (Si/Al = 385). The extra reticular cation most present is hydrogen and the only detectable metal cation (Na^{+}), is present in very small quantities (see Table SI2). For these reasons, Fe was introduced in the USY zeolite by the described impregnation method. A certain oxidation of Fe^{2+} is suggested by the color change of the powder from green, typical of octahedrally coordinated Fe^{2+}, to yellow-brown typical of octahedrally coordinated Fe^{3+}.

When Fe-USY is subjected to thermal treatments under a reducing atmosphere, the following phenomena are likely to occur (Kanari et al., 2018).

1) Dehydration of the zeolite and the hydrated iron salt.
2) Thermal decomposition of the iron salt, accompanied by removal of gaseous species.
3) Formation of reduced iron species.

This last point occurs to a different extent at the three different temperatures (500, 600, 750 °C) selected for the thermal treatment of zeolite Fe-USY, which results in the production of the materials to be tested as catalyst in the photo-Fenton oxidation of phenol in water (Fe-USY500°C-2h, Fe-USY600°C-2h and Fe-USY750°C- 2h). Reduction temperatures below 500 °C result in a limited reduction and insufficient amount of Fe_3O_4 whereas temperatures higher than 750 °C would favor fayalite formation (Pansini et al., 2017; Zieliń et al., 2010; Tahari et al., 2019; Tiernan et al., 2001). The determination of Fe content was performed by Atomic absorption spectroscopy. The Fe concentration was found to be 7.2% by weight for the Fe-USY sample and 10.6% by weight in the Fe-USY500°C-2h, Fe-USY600°C-2h and Fe-USY750°C- 2h catalysts. The difference in iron content between impregnated zeolite and those subjected to reduction treatment is related to the decomposition of Fe salt and the evolution of the zeolitic water.

3.2. Structural, surface and textural characterization

Fig. SI5 shows the XRD pattern, collected as a preliminary test on laboratory instrument, of the original USY commercial zeolite, Fe-USY, Fe-USY500°C-2h, Fe-USY600°C-2h and Fe-USY750°C-2h samples.

The pattern collected on the sample USY matches clearly with that of an ultra-stable dealuminated Y zeolite. The contact between the USY zeolite and the saturated ferrous sulphate solution induced the crystallization of four different Fe sulphate phases with different stoichiometry, specifically: ferricopiapite $Fe^{3+}_{4.66}(SO_4)_6(OH)_2\bullet 20(H_2O)$, hydronium Jarosite $(H_3O)Fe_3(SO_4)_2(OH)_6$, melanterite $Fe^{2+}(SO_4)\bullet 7(H_2O)$ and butlerite $Fe^{3+}(SO_4)\ (OH)\bullet 2(H_2O)$.

From the normalization of the intensities of the pattern before and after the contact with the Fe solution, Fig. SI6, we can observe we have only slight changes in the peak's intensity ratio; thus, we can conclude we have only slight structural modification occurred. Based on the available data, it appears that all the iron present in the impregnated sample, Fe-USY, crystallizes as the sulphate phases and, probably, as amorphous oxides and hydroxides.

To overcome the known problem of Fe fluorescence under Cu radiation, detailed analyses of the temperature-treated samples have been performed exploiting synchrotron radiation. X-ray diffraction patterns with the indication of the reflection of the identified phases are reported in Supplementary information (Fig. SI1-3), while the results of quantitative phase analyses performed after Rietveld Refinement are reported in Table 1.

Quantitative phase analysis showed the presence of a significant amount of amorphous phase on the sample, probably resulting from the dealumination process in agreement with the analyses reported by the authors (Liu et al., 2022; Shirvani et al., 2019).

Table 1
Results of quantitative phase analyses (wt. %). Error in brackets is referred to the last digit (first decimal).

		USY	Fe-USY500°C-2h	Fe-USY600°C-2h	Fe-USY750°C-2h
USY	SiO_2	71.6 (1)	48.0 (1)	42.0 (1)	25.4 (7)
Fe	Fe^0		0.3 (2)	4.3 (6)	5.8 (3)
Magnetite	Fe_3O_4		19.4 (7)	10.7 (6)	1.2 (4)
Fayalite	Fe_2SiO_4		2.7 (7)	1.3 (6)	14.0 (7)
Pyrrhotite	$Fe_{(1-S)}S$		3.9 (5)		
Amorphous phase		28.4 (1)	25.0 (1)	42.0 (1)	53.6 (8)

All the treated samples heated at high temperatures show the appearance of different Fe-bearing phases: fayalite, metallic Fe and magnetite. A Fe sulphide (pyrrhotite) is present only in the sample treated at a lower temperature (500 °C). The width of the Fe-bearing phases peak indicates the presence of nanometric diffraction domains. From the data in Table 1, an increase in the amount of Fe^0 and a simultaneous decrease in the magnetite content can be observed as the heat treatment temperature is raised. Fayalite content also increases with temperature, the higher value observed for the sample treated at 500 °C with respect to that found at 600 °C could result from a slight overestimation due to refinement. Indeed, the large width observed for fayalite peaks, indicating the presence of nanocrystalline phases, makes the refinement extremely challenging.

The quantitative phase analysis reveals another result that deserves some consideration. Although USY zeolite is characterized by high thermal stability, an increase in amorphous content is observed for heat-treated samples. This result can be related to the impregnation process with aqueous solutions of iron salts, which may induce a decrease in phase stability. A similar result has already been reported by other authors indicating that impregnation with iron to some extent damages the zeolitic structure. A decrease in the crystalline phase corresponding to almost 50% was reported by Shirvani et al. for an iron content of 5% by weight (Shirvani et al., 2019). Similar findings were reported by Mohiuddin et al. with a ZSM-5 zeolite impregnated with Fe at 5 wt% (Mohiuddin et al., 2018). In our case, the effect is less marked indicating the effectiveness of the preparation method.

XPS analysis has been conducted on samples: Fe-USY, Fe-USY500°C-2h, Fe-USY600°C-2h and Fe-USY750°C-2h before catalytic tests. Survey scans were performed firstly to check the sample surfaces chemical composition (see Fig. SI7-a).

In Table 2, the relative atomic concentration of both the impregnated and heat-treated samples is reported. Each sample shows C, O, Si and Fe photoelectron peaks, as expected, in slightly different concentrations, according to the specific thermal treatments. Sample Fe-USY is the only one that shows also the presence of N1s and S2p peaks. According to D. Verboekend et al. (2012), commercial USY zeolites can be obtained by dealumination procedures, which can involve HNO_3 (severe process) or H_4EDTA (mild process); both of them can play the role of N precursors, which can be a remnant of these procedures. If we look at the position of N1s peak (~402 eV), this can be assigned to protonated amine or quaternary ammonium bonds. Regarding S2p presence, this is a residue of the sulphate salt precursor, used for the impregnation procedure. N and S signals were no more detected in the thermally treated samples. We have also calculated Fe/Si ratio, according to their relative atomic concentration, finding out that the sample that possesses the highest amount of Fe, in the upper surface, is Fe-USY500°C-2h. To get more information regarding iron oxidation states and their evolution, we performed HR scans in the Fe2p doublet region: for the sake of simplicity, hereafter, we will refer only to peak $Fe2p_{3/2}$, since each comment can be easily translated to its related peak $Fe2p_{1/2}$ ($\Delta = 13.1$

Table 2
Relative atomic concentration calculated by XPS analysis and $Fe2p_{3/2}$ peak position and relative FWHM parameters.

Sample	Relative atomic concentration [at.%]						Fe2p HR signal [eV]	
	C1s	O1s	Si2p	Fe2p	Others	Fe/Si	$Fe2p_{3/2}$	FWHM
Fe-USY	10.4	61.7	21.9	2.3	N: 0.9 S: 2.8	0.11	711.8	3.4
Fe-USY500°C-2h	5.4	64.2	26.6	3.8	–	0.14	711.3	2.8
Fe-USY600°C-2h	6.0	66.8	25.1	2.1	–	0.08	711.3	2.8
Fe-USY750°C-2h	9.8	61.1	27.2	1.9	–	0.07	711.2	3.5

eV). In Fig. SI7-b we have reported Fe2p doublets for all samples. Sample Fe-USY shows a peak ($Fe2p_{3/2}$) at the highest binding energy (711.8 eV), as reported in Table 2, with quite a big FWHM (3.4 eV). The shape of this peak is due to the convolution of different components, since the Fe signal is made up of multiplet splitting, as reported by A. P. Grosvenor et al. (2004). This behavior, together with the presence of surface peaks and shake-up satellites, makes the fitting procedure quite complex, especially when more than one oxidation state is present. According to D. Brion detailed study (Brion, 1980), related to surface degradation of Fe-containing material due to air or water exposure, there is a clear trend that moves the peak maximum towards higher binding energies, when Fe oxidation state increases. For example, $FeSO_4$ is reported at 711.2 eV, while $Fe_2(SO_4)_3$ is shifted to 713.5 eV. If we compare the shape of Fe signal for Fe-USY sample, with the ones obtained for the thermally treated ones, we can easily see a huge difference, not only related to the main peak position (see Table 2), but also to their shape. Samples Fe-USY500°C-2h and Fe-USY600°C-2h possess the typical shape due to iron in a Fe_3O_4 compound, as reported by I. Gomez et al. (Gó et al., 2019), with a weak satellite located around 719.0 eV, due to Fe^{3+} coordination. Fe-USY sample, instead, does not show a well-defined satellite, because the region at higher binding energies is occupied by the components due to $FeSO_4$ chemical shift. This assumption is further confirmed by the presence of S signal, as previously highlighted in the survey spectrum. From HR analysis in the S2p region, we have found out that the peak position (at 169.4 eV) is due to SO_4 group, in agreement with $FeSO_4$ presence. If we look at the highest thermal treatment, we can see that the Fe^{3+} satellite is no more evident and that a shoulder is now present around 715 eV, which is due to Fe^{2+} satellite (Gao et al., 2010). If we consider only the thermally treated samples, from Table 1, we can see that the position of the main peak is almost constant, while the FWHM is increased in the latter sample, due to the increase in the Fe^{2+} component, in agreement with XRD analysis, which reports the reduction of Fe, with temperature increase. The metal component (706.7 eV), which has been clearly evidenced by XRD measurements, has not been detected by XPS analysis in all the samples. This can be justified by the fact that XPS analysis is extremely surface sensitive (10 nm nominal escape depth). Si2p region has been also investigated (spectra not reported), to check for the Si oxidation state. All the samples show a peak in the range (103.8–104.1) eV, with a single component, due to SiO_2 chemical shift.

The N_2 adsorption/desorption isotherms of USY and heat-treated samples, Fe-USY500°C-2h, Fe-USY600°C-2h, Fe-USY750°C-2h, are shown in Fig. SI8. For all samples, the shape of the isotherm resembles a combination of Type I and Type II (Singh and Kalamdhad, 2011), with a hysteresis loop of type H4. The first section of the adsorption branches up to P/P0 = 0.05 is characterized by a very steep increase in the amount of adsorbed N_2 relative to the filling of the micropores (of width $\leq$1 nm). The shape of the isotherm for P/P0 values greater than 0.4, with a convexity with respect to the axis in the region of relatively high pressure, can be located in type II. This behavior can be attributed to the presence of large mesopores or a certain degree of macroporosity. Much higher values of N_2 adsorption for the pristine zeolite, USY sample, suggest higher porous volume and specific surface area.

The porosity was assessed for micro and mesopores range up to 50 nm and the analysis of micro/mesoporosity was done by NL-DFT. The pore size distributions, shown in Fig. SI9a are centered around an average value of 0.9 nm in agreement with the value already reported for this high-silica zeolite (https://www.tosohusa.com/products–services/zeolites). From the cumulative curve, Fig. SI9b, it can be seen that most of the porous volume is located in the micropore zone, although a further increase for a pore width greater than 10 nm indicates the presence of a certain fraction of large mesopores. Indeed, the reduction of Al sites, due to the dealumination process, can reduce the long-range order of zeolite, leading to an increase of large mesopores fraction in the range 10–50 nm. An increase that becomes progressively more pronounced as the heat treatment temperature increases. This behavior is also in agreement with the QPA results that indicate a reduction in long-range order zeolite structure for heat-treated samples.

Table SI3 presents the textural parameters obtained by the elaboration of the adsorption/desorption isotherms. In the presence of a microporous material, particularly in the case of a material with mixed porosity, the choice of a rigorous and valuable method to extract the specific surface area is still a very critical issue (Rouquerol et al., 2007). For this reason, we have included both Langmuir and BET specific surface area values in Table SI3. The pristine zeolite shows the highest $S_{Langmuir}$, 1060 $m^2\ g^{-1}$, with a total pore volume value of 0.67 $cm^3\ g^{-1}$. Although possessing a considerable specific surface area, heat-treated samples show lower values than the starting zeolite. This decrease can be related to the decrease in crystallinity as highlighted by the QPA analysis. The Fe-USY600°C-2h sample is out-trend, with higher $S_{Langmuir}$ and pore volume values. A possible explanation for these data can be found in the heterogeneity of the source materials, where different batches may correspond to slight discrepancies.

Since we are in the presence of a clearly composite adsorption isotherm (type I + type II), which is easily explained by the existence of an appreciable external surface that adds its effect to that of the micropores, we have reported in Table SI3 the values of the external surface calculated by the t-plot method. The trend in external surface area values follows that of the specific surface area, being higher in pristine zeolite. In conclusion, all the samples consist mainly of narrow micropores, with small hints of mesopores, with increasing its percentages from 500 °C to 750 °C thermal treatment temperature.

Further insight into the morphology and structure of the catalyst is provided by TEM characterization (Fig. 1) of the Fe-USY500°C-2h sample (which shows the best catalytic activity, as discussed in the following section). Based on TEM images such as Fig. 1a, it is interesting to notice that zeolite domains are decorated with iron-based nanostructures with variable sizes (in the 5–80 nm range). This is proved by Fast Fourier Transforms (FFT) of different regions (Fig. 1b), which confirm the simultaneous presence of a well-oriented USY zeolite crystalline domain ((Kulkarni and Kaware, 2013; Villegas et al., 2016; Saeed and Ilyas, 2013; Mancuso et al., 2022; Kuši et al., 2006; Babuponnusami and Muthukumar, 2011; U. EPA, 2002; Suarez-Ojeda et al., 2008; Quintanilla et al., 2010; Bahadori et al., 2018) zone axis, crystalline model obtained from (http://www.iza-structure.org/databases/) and magnetite ((Graž et al., 2020) ID: 1010369). Spatially-resolved chemical composition analysis through EDX spectroscopy (Fig. 1c and Fig. SI10) provides further corroboration of the previously discussed results. Fig. 1c reports a Z-contrast High-Angle Annular Dark Field (HAADF) STEM image of the same region alongside EDX maps for Si, Fe, O

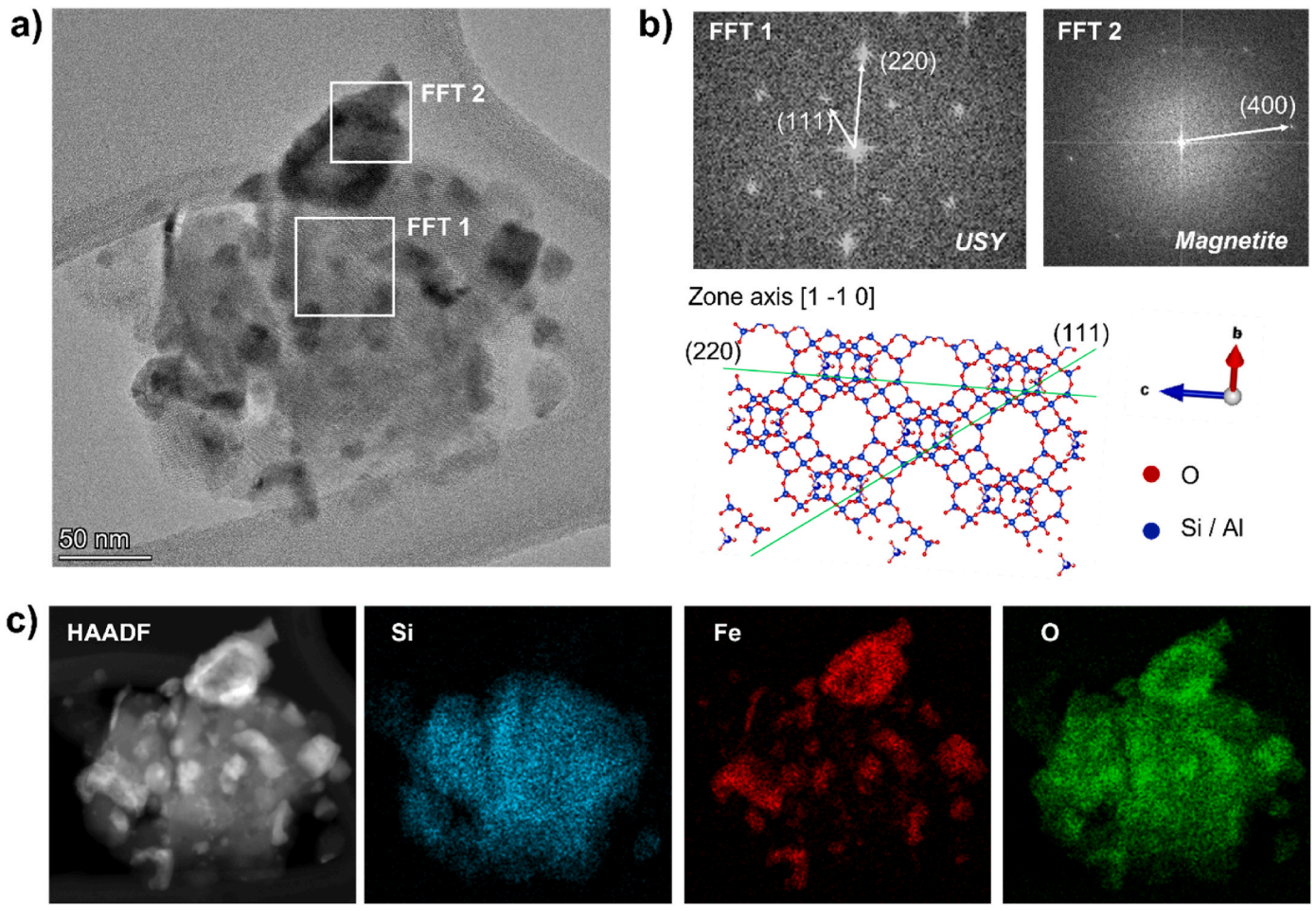

Fig. 1. Representative TEM image (a) for sample Fe-USY500°C-2h, with corresponding Fast Fourier Transforms (FFTs) of two different regions (b). accompanied by the visualization of the crystalline model for the USY zeolite in the (Kulkarni and Kaware, 2013; Villegas et al., 2016; Saeed and Ilyas, 2013; Mancuso et al., 2022; Kuši et al., 2006; Babuponnusami and Muthukumar, 2011; U. EPA, 2002; Suarez-Ojeda et al., 2008; Quintanilla et al., 2010; Bahadori et al., 2018) zone axis. HAADF STEM image and EDX maps for Si, Fe, O are provided in c).

chemical elements. Based on the data presented in Fig. 1c, it is clear that nanostructures with higher average atomic number Z (high-intensity features in the HAADF STEM image) correspond to higher concentrations of Fe. The aforementioned results are a direct confirmation that USY zeolite hosts iron-containing nanostructures primarily in the magnetite crystalline phase, in agreement with the previously discussed XRD quantitative phase analysis.

3.3. Magnetization curve of Fe-USY500°C-2h

An aspect of considerable interest is the possibility of easily separating heterogeneous catalysts from the reaction medium. For this reason, a magnetic characterization was conducted on the best performing catalyst Fe-USY500°C-2h, *vide infra*. The room-temperature hysteresis loop of Fe-USY500°C-2h is shown in Fig. 2a. The measured curve exhibits a small hysteresis (barely visible in the main panel and put in evidence in the lower right panel) and a symmetric, sigmoidal behavior with a clear unsaturation trend at high fields. This feature indicates the presence of a minor paramagnetic phase which can be identified with fayalite (Fe_2SiO_4), as indeed observed by QPA (see Table 1), whose magnetic order-disorder phase transition is around 65 K (Ballet et al., 2012). The coercive field is about 75 Oe, a value compatible with the presence of magnetic nanoparticles within the zeolite. The upper left panel shows the saturating curve (red symbols) obtained by subtracting the paramagnetic signal from the measured data. The maximum magnetization of the Fe-USY500°C-2h is $M_S^{(NC)} \approx$ 15.5 emu/g_{NC} at 17 KOe. After subtracting the paramagnetic contribution, the saturation magnetization of the sample, ascribed to the contribution of Fe^0 and Fe_3O_4 nanoparticles and, to a lesser extent, to ferromagnetic pyrrolithe (characterized by a much lower intrinsic magnetization at room temperature (Schwarz, 1975)), is reduced to $M_S^{(NC)} \approx 14$ emu/g_{NC}. Considering the magnetic nanoparticle fractions determined by QPA for this material (see Table 1), the overall intrinsic saturation magnetization of nanoparticles turns out to be $M_S^{(NP)} \approx 71$ emu/g_{NP}, a result consistent with the predominant weight fraction of Fe_3O_4 over Fe^0 in the sample. The magnetic remanence of the nanocomposite amounts to $M_R \approx 1.85$ emu/g_{NC}. Recalling that the minimum magnetic force F_{mag} exerted on a volume V of a magnetic material, by applying an external magnetic field gradient ∇H, to control the translational motion, is $F_{mag} = M_R\ V\ \nabla H$, it can be concluded that the measured magnetic remanence ensures an effective magnetic separation by using Fe-USY500°C-2h, Fig. 2b.

3.4. Catalytic tests

3.4.1. Effect of sample reduction temperature

Initially, the effect of the reduction temperature on the solar photo-Fenton-oxidation of phenol aqueous solution (50 ppm) was evaluated. The tests were conducted at the spontaneous pH of the phenol solution (pH = 6.4), using a photocatalyst dosage equal to 3 g L^{-1} and an initial stoichiometric dosage of H_2O_2 (Fig. SI11). The TOC removal values achieved after a total treatment time of 120 min, reported in Fig. SI11a,

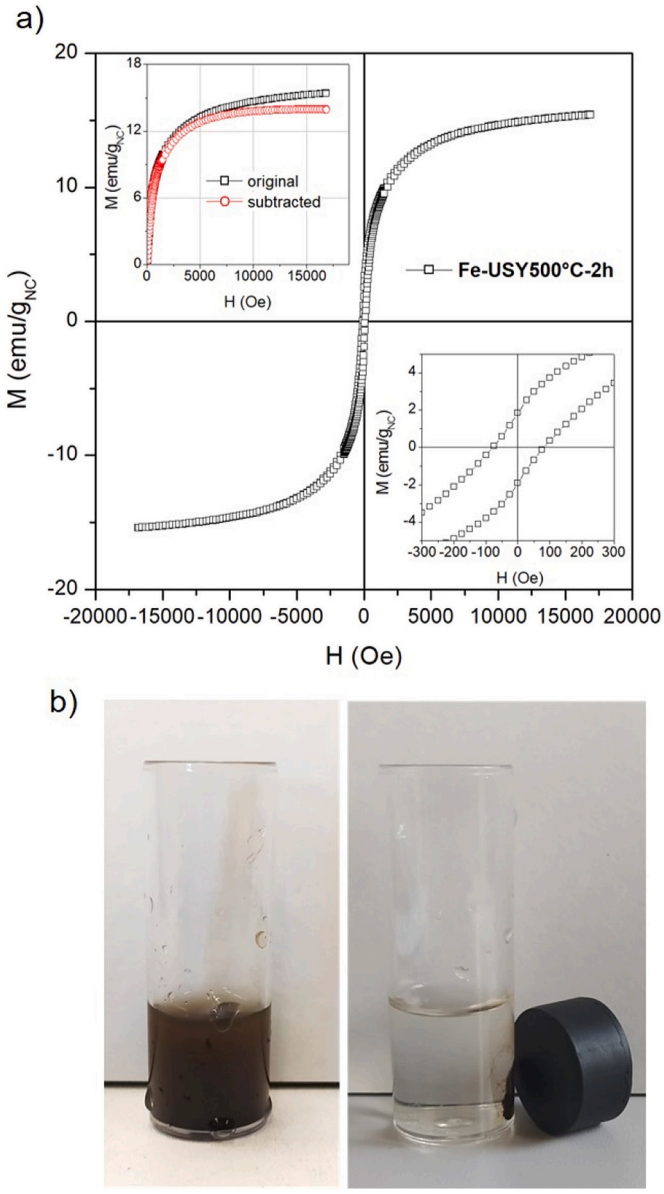

Fig. 2. a) Room-temperature magnetization curve of Fe-USY500°C-2h. Lower right panel: enlargement of the low-field region evidencing magnetic hysteresis; upper left panel: original (measured) and subtracted *M(H)* curves in the first quadrant. b) Aqueous suspension of the Fe-USY500°C-2h sample before and after application of the external magnet, left and right respectively.

show that the optimal sample for phenol mineralization is that reduced at 500 °C. Indeed, the TOC removal efficiency under solar irradiation for Fe-USY500°C-2h sample was about 48%, higher than that obtained using Fe-USY600°C-2h (43%) and USY750°C-2h (1%).

As shown in Fig. SI11b, complete conversion of the total added hydrogen peroxide was achieved after 120 min on Fe-USY500°C-2h. On Fe-USY600°C-2h, after 60 and 120 min, a lower oxidant consumption, being equal to 49.5 and 75.0 %, was observed. Fe-USY750°C-2h demonstrated, (being H_2O_2 consumption 27.5 and 29.5% at 60 and 120 min, respectively) the ability to consume H_2O_2, in two main processes: (i) the decomposition to H_2O and O_2 and (ii) the oxidation of some iron species to Fe_3O_4, as evinced from QPA of the sample Fe-USY750°C- 2h PF (Table SI4).

Considering the QPA analysis, the amount of magnetite decreased by increasing the reduction temperature. Therefore, based on these results, it is possible to argue that the presence of magnetite is very relevant for the photo-Fenton oxidation to CO_2. Indeed, the H_2O_2 consumption increased with the increase of magnetite content in the samples underlining that the presence of magnetite nanoparticles, as evinced by TEM, at a higher extent promotes both the generation of hydroxyl radicals (which are known as the reactive species in Fenton-like processes) and the decomposition of H_2O_2 to H_2O and O_2 (that is the main side reaction) (Jung et al., 2009).

On the other hand, the strong increase of amorphous phase by increasing the reduction temperature at 750 °C, could also cause a worsening of the photo-Fenton activity. The presence of Fe^0 was higher on the less active photocatalyst.

3.4.2. *Effect of initial pH and stability tests*

Subsequently, the effect of pH on the TOC removal efficiency of the process with the best catalyst (Fe-USY500°C-2h), was explored, operating in acidic conditions, at an initial pH of 4. An acidic 0.1 M solution containing HCl was used to modify the pH of the initial phenol solution. The results, reported in Fig. 3a, show that, at pH = 4, the phenol mineralization was enhanced, achieving a TOC removal equal to about 62%, higher than that obtained (about 48%) at the spontaneous pH of

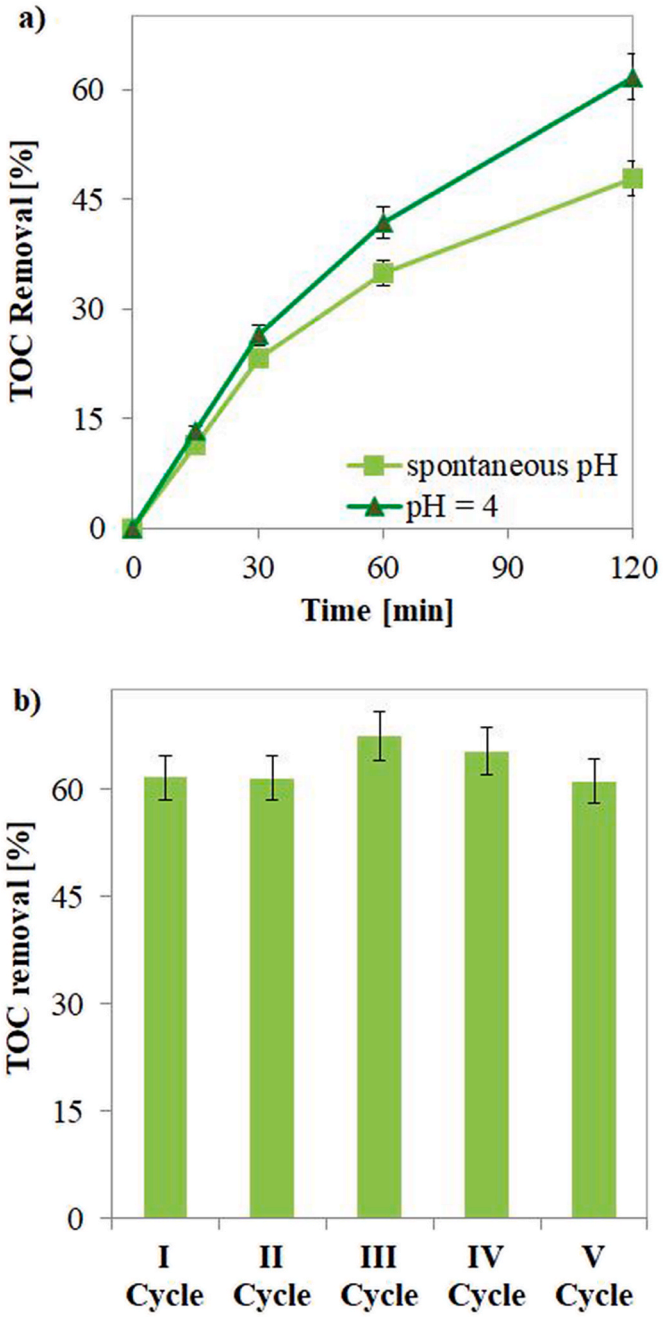

Fig. 3. a) Effect of pH on the TOC removal efficiency by photo-Fenton processes conducted using Fe-USY500°C-2h and H_2O_2 dosage equal to 3 g L^{-1} and 0.253 g L^{-1}, respectively; b) Stability tests of Fe-USY500°C-2h in the phenol mineralization at acidic conditions.

the phenol solution (pH = 6.4).

The role of acidity in heterogeneous photo-Fenton degradation of water pollutants using iron-based catalysts was investigated, evidencing optimal performances in acidic conditions (Litter and Slodowicz, 2017; Shi et al., 2020; Dhahawi Ahmad et al., 2020). Considering such literature papers, the higher performances observed at pH = 4 are retained ascribable to a higher oxidation-reduction potential of hydroxyl radicals (Litter and Slodowicz, 2017; Li et al., 2016). In addition, the mechanism which involves heterogeneous iron species foreseen the oxidation of ≡Fe $^{2+}$ by H_2O_2 to generate •OH radicals (Eq. 2) able to degrade the pollutant, and the so-generated ≡Fe^{3+} requires to be reduced to recover Fe^{2+}, closing the catalytic cycle. The latter reaction can be obtained: i) by H_2O_2 generating a H^+ and the hydroperoxide radical, less oxidant than hydroxyl radical (Eq. 2), or ii) by H_2O, promoted by photon absorption, which results in a further •OH (Eq. 4). As a consequence, the role of acidity is retained to be the prevention of ≡Fe^{3+} and OH^- to form an iron complex (Eq. (5)), yielding higher reducibility of ≡ Fe^{3+} to ≡ Fe^{2+} (Eq. (6)), necessary for the formation of highly active hydroxyl radicals.

$$\equiv Fe^{2+} + H_2O_2 \rightarrow \equiv Fe^{3+} + OH^- + {}^{\cdot}OH \quad \text{Eq (2)}$$

$$\equiv Fe^{3+} + H_2O_2 \rightarrow H^+ + HOO^{\cdot} + \equiv Fe^{2+} \quad \text{Eq (3)}$$

$$\equiv Fe^{3+} + H_2O + h\nu \rightarrow \equiv Fe^{2+} + {}^{\cdot}OH + H^+ \quad \text{Eq (4)}$$

$$\equiv Fe^{3+} + OH^- \rightarrow \text{Iron Complex} \quad \text{Eq (5)}$$

$$\text{Iron complex} + H^+ \rightarrow \equiv Fe^{3+} + H_2O \quad \text{Eq (6)}$$

On the other hand, at higher pH values, the decomposition of H_2O_2 into O_2 is favored, reducing the production of hydroxyl radicals (Litter and Slodowicz, 2017).

To evaluate the stability of Fe-USY500°C-2h, five cycles of experimental tests were conducted under the same acid conditions, recovering the sample through magnetic separation and recycling after each test without any pre-treatment. The obtained results confirmed the stability of the sample (Fig. 3b) since the mean value of TOC removal was 63 ± 5%.

3.4.3. *Effect of initial H_2O_2 dosage*

Subsequently, the influence of the initial dosage of hydrogen peroxide on the reaction system, using Fe-USY500°C-2h sample and initial pH = 4, was analyzed by varying this parameter in the range of 0.266–0.798 g L^{-1}. Two additions of oxidant of equal dosage were performed at fixed times: initial time, and 60 min of solar irradiation.

The influence of hydrogen peroxide dosage on the photo-Fenton activity depends on the generation of hydroxyl radicals (•OH) and their conversion into lower oxidants hydroperoxide radicals ($HO_2^{\bullet}$).

As reported in Fig. SI12a, the mineralization of the pollutant was increased varying H_2O_2 dosage from 0.266 g L^{-1} to 0.532 g L^{-1} which is due to the increase of hydroxyl radicals produced. However, increasing the dosage above 0.532 g L^{-1} negatively affected phenol mineralization. This phenomenon is assigned to the auto-decomposition of hydrogen peroxide to oxygen and water and the transformation of hydroxyl radicals into hydroperoxide radicals. (Eq. (7) and (8)) (Ebrahiem et al., 2017):

$$2\,H_2O_2 \rightarrow 2\,H_2O + O_2 \quad \text{Eq (7)}$$

$${}^{\cdot}OH + H_2O_2 \rightarrow HO_2^{\cdot} + H_2O \quad \text{Eq (8)}$$

Hence, the optimal initial dosage of oxidant is equal to 0.532 g L^{-1}. Indeed, for this value of the hydrogen peroxide dosage, the complete oxidant consumption (Fig. SI12b) and the maximum mineralization (TOC percentage removal equal to 98% in Fig. SI12a) after 120 min of simulated sunlight irradiation were obtained.

3.4.4. *Effect of ion species in water matrix*

For a potential scale-up of a heterogeneous photo-Fenton water treatment process, it is crucial to assess the impact of the water matrix nature on process performance, especially the potential scavenging role of inorganic ions, which are frequently present in wastewater (Ribeiro et al., 2019; Cheng et al., 2023).

For this reason, an additional test employing Fe-USY500°C-2h was carried out using a tap water sample (Table SI1) contaminated by phenol at the optimal operative parameters, in order to compare the results of this test to those obtained in the photo-Fenton experiment in distilled water at the same conditions.

The results reported in Fig. 4a show the effectiveness of the system also in the degradation of phenol in the presence of inorganic ionic

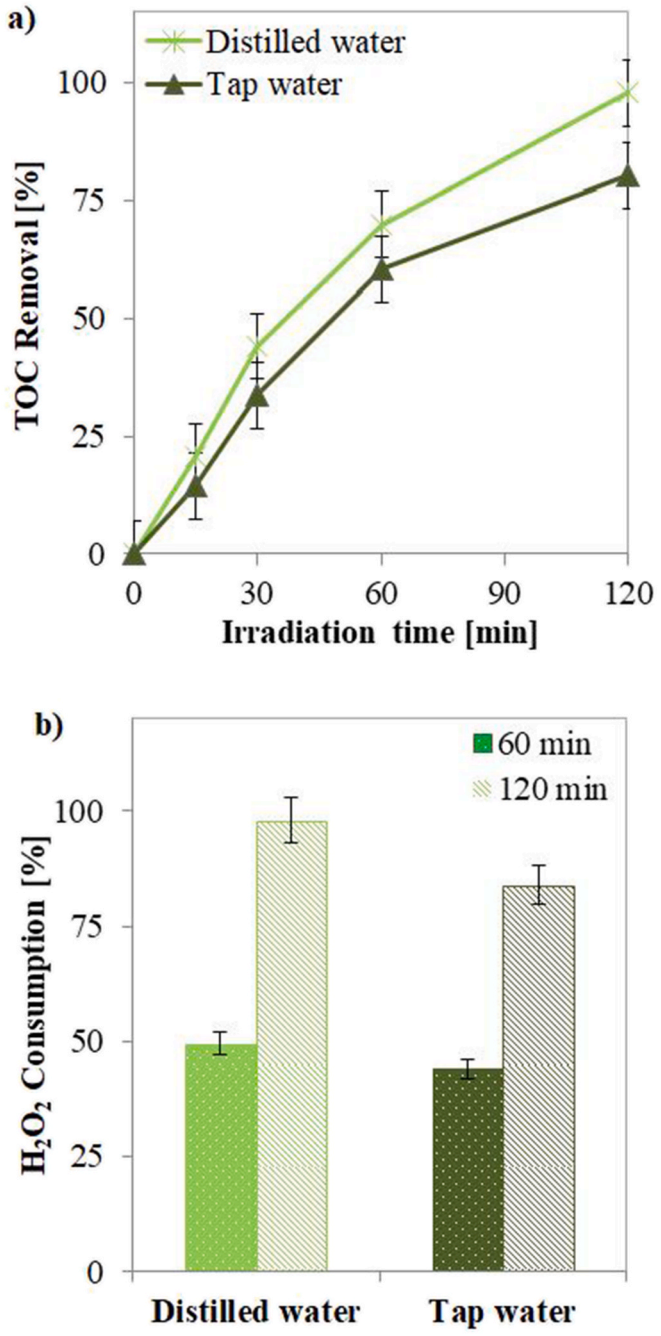

Fig. 4. a) Trend of TOC removal efficiency under solar irradiation on Fe-USY500°C-2h in the presence of distilled and tap water; b) H_2O_2 consumption after 60 and 120 min under solar irradiation on Fe-USY500°C-2h in presence of distilled and tap water.

species. However, the photo-Fenton activity slightly decreased in the case of the tap water matrix, both in terms of mineralization (Fig. 4a) and consumption of hydrogen peroxide (Fig. 4b). Indeed, the Fe-USY500°C-2h sample in the presence of the ions contained in tap water showed a TOC removal after 120 min equal to 80%, and a decrease in the consumption of hydrogen peroxide, confirming the hypothesis that the presence of ions contained in the tap water can act as radical scavengers (Cheng et al., 2023).

3.4.5. Iron leaching tests

It must be remarked that the leaching of iron in the overall tests of H_2O_2-assisted phenol photodegradation with the optimal sample (Fe-USY500°C-2h) was only 1 ppm, a value below the standard limits for the treated water discharge set by Italian regulation for effluent discharge into surface water (≤2 ppm) (annex 5, third part, D.Lgs n. 152/2006). The contribution of homogeneous photo-Fenton reaction should be thus excluded. Furthermore, it should be noted that leaching phenomena are more important (up to 4.4 ppm) than the other iron-impregnated Y zeolites reported in the literature (Ayoub et al., 2018). As a general comment, we obtained phenol mineralization performances better than those reported in the literature dealing with the use of iron-impregnated zeolite catalysts. For instance, compared with the results reported in (Ayoub et al., 2018), we have obtained a considerable improvement in the photocatalytic performance of the Fe-zeolite considering the lower iron leaching, the higher initial phenol concentration, and the cheaper irradiation carried out with simulated sunlight.

3.4.6. Comparison between the heterogeneous and the homogeneous photo-fenton

Finally, a homogeneous photo-Fenton test was carried out using the optimal operating conditions identified for the heterogeneous photo-Fenton process: initial pH equal to 4, initial dosage of H_2O_2 equal to 0.533 g L^{-1}, Fe^{2+} ions dosage equal to 0.216 g L^{-1} (using 107.53 mg of ferrous sulphate heptahydrate). This iron dosage corresponds to the total amount of Fe ions loaded in the heterogenous photocatalyst at a dosage of 3 g L^{-1} in the reaction system.

The experimental data presented in Fig. SI13a and SI13b highlight that the solar heterogeneous process shows both activity in phenol mineralization and H_2O_2 consumption comparable to the homogeneous process, evidencing that the heterogeneous Fe-USY500°C-2h catalyst could be a valid alternative to the traditionally used homogeneous catalyst.

3.4.7. Evaluation of the reaction mechanism

Subsequently, to unravel the mechanism of the heterogeneous photo-Fenton system under simulated sunlight, tests in the presence of scavenger molecules were conducted using the optimal identified conditions (initial phenol concentration: 50 mg L^{-1}; pH = 4; initial H_2O_2 dosage: 0.532 g L^{-1}).

In detail, the scavenger probe molecules used in the activity tests were: isopropanol (IPA, 10 mmol L^{-1}) for hydroxyl radicals (Sacco et al., 2021), and silver nitrate (SN, 10 mmol L^{-1}) for electrons (Schneider et al., 2020; Saragi et al., 2018). Indeed, it must be remarked that magnetite possesses an interesting band gap energy (1.8–2.2 eV) making it suitable to be excited by solar light (Abadiah et al., 2019), so the contribution of photocatalysis in the reaction system has been evaluated (Fig. SI14). The silver nitrate was chosen as a scavenger for electrons because Ag^+/Ag^0 reduction potential ($E^0 = +0.80$ eV vs. SHE) is higher than Fe^{3+}/Fe^{2+} reduction potential ($E^0 = +0.77$ eV vs. SHE) (Xing et al., 2018; Dolfing et al., 2006). For this reason, the electrons photo-promoted in the conduction band of Fe_3O_4 (Al-Anbari et al., 2016) preferentially reduce Ag^+ into Ag^0, avoiding the reduction of Fe^{3+} to Fe^{2+}. Furthermore, to observe the influence of the presence of superoxide ions inside the system, a test was conducted under the same operating conditions but feeding an air stream instead of nitrogen into the reactor, with a flow rate of 142 STP cm^3 min^{-1}.

From the results, shown in Fig. 5, it emerged that the degradation of the phenol occurs essentially starting from the hydroxyl radicals ($^{\bullet}OH$) produced within the contaminated solution generated by the synergistic action of the Fe^{3+}/Fe^{2+} present in the magnetite, the hydrogen peroxide, and, in less extent, the positive holes formed by the Fe_3O_4 activation by solar light (Khan et al., 2020). Indeed, the experimental test conducted in the presence of IPA showed a decrease of 96% in TOC removal after 180 min under solar irradiation.

It must be remarked that the reaction $H_2O_2 + h\nu \rightarrow 2\ ^{\bullet}OH$, doesn't take place in our system (blank test in the absence of photocatalyst is reported in Fig. SI15). Indeed, a higher energy UV irradiation ($\lambda < 380$ nm) is necessary for the decomposition of H_2O_2 into hydroxyl radicals,

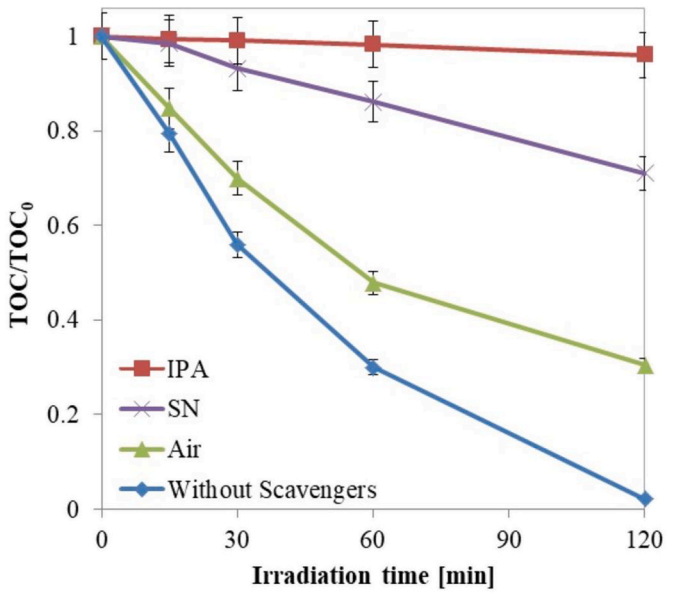

Fig. 5. Trend of normalized TOC with respect to its initial value (TOC_0) as a function of irradiation time obtained for the tests with the optimal conditions in the presence of IPA, SN, Air, and without the scavengers.

which cannot occur when irradiating the reaction system with solar light (Cataldo, 2014).

On the other hand, the data collected from the activity test with air fed to the reactor underlines that the presence of superoxide radical anion ($O_2^{-\bullet}$) decelerates the oxidation reactions of phenol and its intermediates. Indeed, the continuous blowing of air into the reaction system leads to the formation of $O_2^{-\bullet}$. In the reaction system, this radical favors the generation of hydroperoxide radicals which have a lower oxidizing power than hydroxyl radicals (Mancuso et al., 2022). Moreover, the generation of superoxide subtracts electrons for the regeneration of Fe^{2+} ions, being the O_2/H_2O reduction potential greater respect to the Fe^{3+}/Fe^{2+} reduction potential (+1.23 eV and +0.77 eV vs. SHE, respectively) (Pegis et al., 2015; Zhang and Zhou, 2019).

Therefore, based on the results reported in Fig. 5, it is possible to argue that the photo-Fenton mechanism occurring using Fe-USY500°C-2h in the optimized operative conditions and feeding nitrogen to the reactor, is as follows:

$$Fe_3O_4 + h\,\nu \rightarrow h^+ + e^- \quad \text{Eq (9)}$$

$$\equiv Fe^{2+} + H_2O_2 \rightarrow \equiv Fe^{3+} + OH^- + {}^{\cdot}OH \quad \text{Eq (2)}$$

$$\equiv Fe^{3+} + e^- \rightarrow \equiv Fe^{2+}\ [(\text{Minella et al., 2014})] \quad \text{Eq10}$$

$$\equiv Fe^{3+} + H_2O_2 \rightarrow H^+ + HOO^{\cdot} + \equiv Fe^{2+} \quad \text{Eq (3)}$$

$$\equiv Fe^{3+} + H_2O + h\,\nu \rightarrow \equiv Fe^{2+} + {}^{\cdot}OH + H^+ \quad \text{Eq (4)}$$

$$OH^- + h^+ \rightarrow {}^{\cdot}OH \quad \text{Eq (11)}$$

$$C_6H_5OH + {}^{\cdot}OH \rightarrow \text{intermediates} \rightarrow CO_2 + H_2O \quad \text{Eq (12)}$$

3.5. Post reaction characterization

The most performing catalyst has been characterized also after the catalytic test to assess the stability of the catalyst after the photo-Fenton (PF) process. The XRD diffraction patterns are reported in Fig. SI16.

Table SI55 shows the results of the quantitative phase analysis on the sample treated at 500 °C after its use as a catalyst for the photo-Fenton oxidation of phenol in water, Fe-USY500°C-2h PF. The comparison with the data in Table 1 appears very interesting.

The most impressive result comes from the Fe_3O_4 content, which remains virtually constant during the photo-Fenton reaction, being Fe-USY500°C-2h PF (19.2 wt %) compared to the Fe-USY500°C-2h sample (19.4 wt %). This agrees with the finding that the catalyst is stable up to five cycles. XPS measurements have been also performed on sample Fe-USY-500°C-2h after the photo-Fenton reaction. Starting from the survey spectrum (see Fig. SI17-a) we can see that only C, O, Fe and Si signals have been detected. The element's relative atomic concentration is the following: C1s 19.1 at. %, O1s 55.8 at. %, Si2p 21.6 at. % and Fe2p 3.5 at.%. There is a slight increase in the C content, compared with the thermally treated samples before PF reaction, which can be related to residues due to phenol interaction. To further assess the stability of the catalyst we checked and compared the Fe2p signal of Fe-USY500°C-2h before and after the PF reaction: as reported in Fig. SI17-b, we can easily see that the two experimental curves are perfectly overlapped, showing the well-known satellite at 719 eV due to Fe^{3+} component in the Fe_3O_4 typical signal shape. We have also added the signal acquired from the metal reference, to underline the absence of the Fe^0 component at 706.7 eV, in both the Fe-USY-500°C-2h and Fe-USY500°C-2h-PF signals. As a final check, we compared also Si2p signals from before and after PF reaction for sample Fe-USY500°C-2h (Fig. SI17-c). The two curves are well superimposed, with the peaks centroids located at 103.9 eV for both curves, showing a stable chemical shift before and after the reaction. Nevertheless, there is a slight difference between the two curves, since the signal before PF reaction has a 1.9 eV FWHM, while the post reaction one possesses a 2.1 eV FWHM. This slight broadening in the post-reaction curve can be ascribed to several causes (Krishna and Philip, 2022): surface charging due to a more insulating surface (extrinsic broadening); inhomogeneities in the material which correspond to a greater degree of disorder in the matrix structure, by creating new defects, which behave as scatter points in which photoemitted electrons lose their kinetic energy, thus resulting in an increase in the binding energy scale (intrinsic broadening).

The adsorption of N_2 on the Fe-USY500°C-2h PF sample shows incontrovertibly that the reaction environment for the photo-degradation of phenol does not change the textural properties of the catalyst Fe-USY500°C-2h. Indeed, the Langmuir surface area value obtained is 628 m^2g^{-1}, which is higher than the pre-reaction value (see Table SI3). According to this finding, the pore size distribution in Fig. SI18, shows that the main peak is still located at 0.9 nm, even if it appears less sharper. The cumulative pore volume (insert in Fig. SI18) shows an increased presence of large mesopores compared with the pre-reaction sample.

TEM characterization of the Fe-USY500°C-2h PF sample confirms that the morphology and structure of the catalyst do not suffer significant evolution after cycling. Based on representative images of the sample after cycling (such as Fig. SI19a), the nanostructures are still present at the surface of USY zeolite domains. FFT analysis of the single nanostructures (Fig. SI19b) provides evidence that the magnetite crystalline structure is retained after cycling, in agreement with XRD results.

4. Conclusions

In this work, for the first time, an ultra-stable Y (USY) zeolite with a high silicon/aluminum ratio (Si/Al molar ratio = 385), was used to entrap reduced iron species, which exhibit remarkable catalytic activity in the heterogeneous photo-Fenton removal of phenol under solar light. The adopted vacuum impregnation procedure, specifically set up for this work, and the subsequent heat treatment in a reducing atmosphere proved to be reasonably respectful of the zeolite framework, which was scarcely damaged, in contrast to literature data. The synthesis method resulted in the formation of nano-sized magnetite particles with a content that can be manipulated through the heat treatment temperature. In detail, the higher amount is observed at 500 °C and then gradually drops as heat treatment increases, towards the formation of metallic iron and

fayalite. The best photo-Fenton performances at the spontaneous pH of the aqueous phenol solution (pH = 6.4) were achieved with the catalyst obtained through thermal treatment at 500 °C (Fe-USY500°C-2h). More in detail, the total organic carbon (TOC) removal under solar irradiation for Fe-USY500°C-2h sample was about 48%, higher than that obtained using Fe-USY600°C-2h (43%) and USY750°C-2h (1%). The better performances observed for the Fe-USY500°C-2h catalyst were ascribed to its higher magnetite content and H_2O_2 consumption, allowing to enhance the generation of hydroxyl radicals, responsible for phenol removal by photo-Fenton process under solar light. Noticeably, from the photo-Fenton tests performed to assess the influence of operating conditions, it was found that the complete phenol mineralization was achieved in 120 min of irradiation in acidic conditions (pH = 4) and using an H_2O_2 dosage of 0.532 g L^{-1}.

The magnetic features of Fe-USY500°C-2h sample allow an easy separation of catalyst particles from the treated solution through magnetic separation. The recovered sample was reused five times, showing no significant worsening of phenol removal performances. The stability of Fe-USY500°C-2h was confirmed by the physicochemical characterization of the sample after the reaction, which unequivocally shows that the structural, surface and textural properties were maintained. Fe-USY500°C-2h catalyst was proven to be effective in phenol removal also in tap water (TOC removal = 80%). The photo-Fenton experiments carried out in the presence of scavenger probe molecules revealed that hydroxyl radicals play the main role in the removal of phenol, allowing to establish the action of entrapped magnetite in the reaction mechanism.

Finally, the heterogeneous Fe-USY500°C-2h catalyst showed similar activity to the homogenous photo-Fenton process, underlining the possibility of application of the magnetically recoverable catalyst optimized in this work as an alternative to the traditionally homogeneous catalysts.

Overall, the found photo-Fenton reactivity of Fe-USY500°C-2h opens to cheaper applications driven by solar light to carry out the phenol removal with industrially scalable photo-Fenton catalysts owing to the synthesis method setup.

Credit author statement

Serena Esposito, Vincenzo Vaiano, Diana Sannino, Michele Pansini: Conceptualization, Methodology, Supervision, Validation, Writing-Reviewing and Editing; Paolo Allia, Rossella Arletti, Marco Fontana, Micaela Castellino: Investigation, Methodology, Formal analysis, Writing - Original Draft; Olimpia Tammaro, Nicola Morante: Formal Analysis, Investigation, Data Curation, Gabriele Barrera, Paola Tiberto, Antonello Marocco, Riccardo Fantini: Formal analysis, Visualization, Validation.

Declaration of competing interest

The authors declare that they have no known competing financial interests or personal relationships that could have appeared to influence the work reported in this paper.

Data availability

Data will be made available on request.

Acknowledgements

Transmission Electron Microscope (TEM) was purchased with funding from the "Ministero dell'Università e della Ricerca (MUR)" (Italy) under the "Dipartimento di Eccellenza 2018–2022" program.

Dr. Marco Allione is cordially acknowledged for the experimental TEM support given for the realization of the present study.

Appendix A. Supplementary data

Supplementary data to this article can be found online at https://doi.org/10.1016/j.chemosphere.2023.140400.

References

Abadiah, N.M., Yuliantika, D., Hariyanto, Y.A., Saputro, R.E., Taufiq, A., Soontaranoon, S., 2019. Nanostructure, band gap, and antibacterial activity of spinel Fe2MO4/OO magnetic fluids. In: IOP Conference Series: Earth and Environmental Science. IOP Publishing, 012064.

Al-Anbari, R., Al-Obaidy, A.H., Abd, E., 2016. Photocatalytic activity of Fe3O4 under solar radiation. Mesopotamia Environmental Journal 2, 41–53.

Ayoub, H., Roques-Carmes, T., Potier, O., Koubaissy, B., Pontvianne, S., Lenouvel, A., Guignard, C., Mousset, E., Poirot, H., Toufaily, J., 2018. Iron-impregnated zeolite catalyst for efficient removal of micropollutants at very low concentration from Meurthe river. Environ. Sci. Pollut. Control Ser. 25, 34950–34967.

Babuponnusami, A., Muthukumar, K., 2011. Degradation of phenol in aqueous solution by fenton, sono-fenton and sono-photo-fenton methods. Clean: Soil, Air, Water 39, 142–147.

Baerlocher, C., McCusker, L.B., Olson, D.H., 2007. Atlas of Zeolite Framework Types. Elsevier.

Bahadori, E., Vaiano, V., Esposito, S., Armandi, M., Sannino, D., Bonelli, B., 2018. Photo-activated degradation of tartrazine by H2O2 as catalyzed by both bare and Fe-doped methyl-imogolite nanotubes. Catal. Today 304, 199–207.

Ballet, O., Brückel, T., Bukowinski, M., Burton, B., Davidson, P., Dolino, G., Fuess, H., Lottermoser, W., Matsui, M., Matsui, Y., 2012. Structural and Magnetic Phase Transitions in Minerals. Springer Science & Business Media.

Bossmann, S., Oliveros, E., Göb, S., Kantor, M., Göppert, A., Lei, L., Yue, P.L., Braun, A., 2001. Degradation of polyvinyl alcohol (PVA) by homogeneous and heterogeneous photocatalysis applied to the photochemically enhanced Fenton reaction. Water Sci. Technol. 44, 257–262.

Breck, D., Smith, J., 1959. Molecular sieves, Scientific American 200, 85–96.

Brion, D., 1980. Photoelectron spectroscopic study of the surface degradation of pyrite (FeS2), chalcopyrite (CuFeS2), sphalerite (ZnS), and galena (PbS) in air and water. Appl. Surf. Sci. 5, 133–152.

Cataldo, F., 2014. Hydrogen peroxide photolysis with different UV light sources including a new UV-LED light source. New Frontiers in Chemistry 23, 99.

Cheng, X., Liang, L., Ye, J., Li, N., Yan, B., Chen, G., 2023. Influence and mechanism of water matrices on H2O2-based Fenton-like oxidation processes: a review. Sci. Total Environ., 164086

Dhahawi Ahmad, A.R., Imam, S.S., Oh, W.D., Adnan, R., 2020. Fe3O4-zeolite hybrid material as hetero-fenton catalyst for enhanced degradation of aqueous ofloxacin solution. Catalysts 10, 1241.

Dolfing, J., Van Eekert, M., Mueller, J., 2006. Thermodynamics of low Eh reactions. In: Proceedings, Fifth International Conference on Remediation of Chlorinated and Recalcitrant Compounds, pp. 22–25. Monterey, CA, USA, May.

Ebrahiem, E.E., Al-Maghrabi, M.N., Mobarki, A.R., 2017. Removal of organic pollutants from industrial wastewater by applying photo-Fenton oxidation technology. Arab. J. Chem. 10, S1674–S1679.

Eisenberg, G., 1943. Colorimetric determination of hydrogen peroxide. Industrial & Engineering Chemistry Analytical Edition 15, 327–328.

Elshorbagy, W., Chowdhury, R., 2013. Water Treatment. BoD–Books on Demand.

Esposito, S., Dell'Agli, G., Marocco, A., Bonelli, B., Allia, P., Tiberto, P., Barrera, G., Manzoli, M., Arletti, R., Pansini, M., 2018. Magnetic metal-ceramic nanocomposites obtained from cation-exchanged zeolite by heat treatment in reducing atmosphere. Microporous Mesoporous Mater. 268, 131–143.

Freyria, F.S., Marocco, A., Esposito, S., Bonelli, B., Barrera, G., Tiberto, P., Allia, P., Oudayer, P., Roggero, A., Matéo-Vélez, J.-C., 2019. Simulated Moon agglutinates obtained from zeolite precursor by means of a low-cost and scalable synthesis method. ACS Earth Space Chem. 3, 1884–1895.

Gao, G., Shi, R., Qin, W., Shi, Y., Xu, G., Qiu, G., Liu, X., 2010. Solvothermal synthesis and characterization of size-controlled monodisperse Fe 3 O 4 nanoparticles. J. Mater. Sci. 45, 3483–3489.

Gómez, I., Cabanzo, R., Mejía-Ospino, E., 2019. Facile method to functionalize graphene oxide with variable load of magnetite nanoparticles. In: Journal of Physics: Conference Series. IOP Publishing, 012037.

Gong, Q., Liu, Y., Dang, Z., 2019. Core-shell structured Fe3O4@ GO@ MIL-100 (Fe) magnetic nanoparticles as heterogeneous photo-Fenton catalyst for 2, 4-dichloro-phenol degradation under visible light. J. Hazard Mater. 371, 677–686.

Gražulis, S., Merkys, A., Vaitkus, A., 2020. Crystallography Open Database (COD), Handbook of Materials Modeling: Methods: Theory and Modeling, pp. 1863–1881.

Grosvenor, A., Kobe, B., Biesinger, M., McIntyre, N., 2004. Surface and Interface Analysis: an International Journal devoted to the development and application of techniques for the analysis of surfaces. Interfaces and Thin Films 36, 1564–1574.

Gualtieri, A.F., Mazzucato, E., Venturelli, P., Viani, A., Zannini, P., Petras, L., 1999. X-ray powder diffraction quantitative analysis performed in situ at high temperature: application to the determination of NiO in ceramic pigments. J. Appl. Crystallogr. 32, 808–813.

Huang, X., Xiao, J., Yi, Q., Li, D., Liu, C., Liu, Y., 2022. Construction of core-shell Fe3O4@ GO-CoPc photo-Fenton catalyst for superior removal of tetracycline: the role of GO in promotion of H2O2 to• OH conversion. J. Environ. Manag. 308, 114613.

Jung, Y.S., Lim, W.T., Park, J.Y., Kim, Y.H., 2009. Effect of pH on fenton and fenton-like oxidation. Environ. Technol. 30, 183–190.
Kanari, N., Menad, N.-E., Ostrosi, E., Shallari, S., Diot, F., Allain, E., Yvon, J., 2018. Thermal behavior of hydrated iron sulfate in various atmospheres. Metals 8, 1084.
Khan, I., Zada, N., Khan, I., Sadiq, M., Saeed, K., 2020. Enhancement of photocatalytic potential and recoverability of Fe 3 O 4 nanoparticles by decorating over monoclinic zirconia. Journal of Environmental Health Science and Engineering 18, 1473–1489.
Koner, D., Schwilk, M., Patra, S., Bieske, E., Meuwly, M., 2020. Full-dimensional ground state potential energy surface, vibrational energy levels, and dynamics. J. Chem. Phys. 153, 044302.
Konstantinou, I.K., Albanis, T.A., 2004. TiO2-assisted photocatalytic degradation of azo dyes in aqueous solution: kinetic and mechanistic investigations: a review. Appl. Catal. B Environ. 49, 1–14.
Krishna, D.N.G., Philip, J., 2022. Review on surface-characterization applications of X-ray photoelectron spectroscopy (XPS): recent developments and challenges. Applied Surface Science Advances 12, 100332.
Kulkarni, S.J., Kaware, J.P., 2013. Review on research for removal of phenol from wastewater. International journal of scientific and research publications 3, 1–5.
Kušić, H., Koprivanac, N., Božić, A.L., Selanec, I., 2006. Photo-assisted Fenton type processes for the degradation of phenol: a kinetic study. J. Hazard Mater. 136, 632–644.
Kwan, W.P., Voelker, B.M., 2003. Rates of hydroxyl radical generation and organic compound oxidation in mineral-catalyzed Fenton-like systems. Environ. Sci. Technol. 37, 1150–1158.
Larson, A.C., Von Dreele, R.B., 1994. Gsas. Report lAUR, pp. 86–748.
Li, W., Wan, D., Wang, G., Chen, K., Hu, Q., Lu, L., 2016. Heterogeneous Fenton degradation of Orange II by immobilization of Fe 3 O 4 nanoparticles onto Al-Fe pillared bentonite. Kor. J. Chem. Eng. 33, 1557–1564.
Litter, M.I., Slodowicz, M., 2017. An overview on heterogeneous Fenton and photoFenton reactions using zerovalent iron materials. J. Adv. Oxid. Technol. 20, 20160164.
Liu, C., Liu, Y., Dang, Z., Zeng, S., Li, C., 2021. Enhancement of heterogeneous photo-Fenton performance of core-shell structured boron-doped reduced graphene oxide wrapped magnetical Fe3O4 nanoparticles: Fe (II)/Fe (III) redox and mechanism. Appl. Surf. Sci. 544, 148886.
Liu, Q., Peng, B., Zhou, Q., Zheng, A., Gao, X., Qi, Y., Yuan, S., Zhu, Y., Zhang, L., Song, H., 2022. Role of iron contaminants in the pathway of ultra-stable Y zeolite degradation. Catal. Sci. Technol. 12, 4145–4156.
Mancuso, A., Morante, N., De Carluccio, M., Sacco, O., Rizzo, L., Fontana, M., Esposito, S., Vaiano, V., Sannino, D., 2022. Solar driven photocatalysis using iron and chromium doped TiO2 coupled to moving bed biofilm process for olive mill wastewater treatment. Chem. Eng. J. 450, 138107.
Manzoli, M., Tammaro, O., Marocco, A., Bonelli, B., Barrera, G., Tiberto, P., Allia, P., Matéo-Vélez, J.-C., Roggero, A., Dantras, E., 2021. New insights in the production of simulated moon agglutinates: the use of natural zeolite-bearing rocks. ACS Earth Space Chem. 5, 1631–1646.
Marocco, A., Dell'Agli, G., Esposito, S., Pansini, M., 2012. Metal-ceramic composite materials from zeolite precursor. Solid State Sci. 14, 394–400.
Minella, M., Marchetti, G., De Laurentiis, E., Malandrino, M., Maurino, V., Minero, C., Vione, D., Hanna, K., 2014. Photo-Fenton oxidation of phenol with magnetite as iron source. Appl. Catal. B Environ. 154, 102–109.
Mohiuddin, E., Mdleleni, M.M., Key, D., 2018. Catalytic cracking of naphtha: the effect of Fe and Cr impregnated ZSM-5 on olefin selectivity. Applied Petrochemical Research 8, 119–129.
Morales, I., Muñoz, M., Costa, C.S., Alonso, J.M., Silva, J.M., Multigner, M., Quijorna, M., Ribeiro, M.R., De La Presa, P., 2020. Induction heating in nanoparticle impregnated zeolite. Materials 13, 4013.
Neamţu, M., Catrinescu, C., Kettrup, A., 2004a. Effect of dealumination of iron (III)—exchanged Y zeolites on oxidation of Reactive Yellow 84 azo dye in the presence of hydrogen peroxide. Appl. Catal. B Environ. 51, 149–157.
Neamţu, M., Zaharia, C., Catrinescu, C., Yediler, A., Macoveanu, M., Kettrup, A., 2004b. Fe-exchanged Y zeolite as catalyst for wet peroxide oxidation of reactive azo dye Procion Marine H-EXL. Appl. Catal. B Environ. 48, 287–294.
Noorjahan, M., Kumari, V.D., Subrahmanyam, M., Panda, L., 2005. Immobilized Fe (III)-HY: an efficient and stable photo-Fenton catalyst. Appl. Catal. B Environ. 57, 291–298.
Oancea, P., Meltzer, V., 2013. Photo-Fenton process for the degradation of Tartrazine (E102) in aqueous medium. J. Taiwan Inst. Chem. Eng. 44, 990–994.
Pansini, M., Dell'Agli, G., Marocco, A., Netti, P.A., Battista, E., Lettera, V., Vergara, P., Allia, P., Bonelli, B., Tiberto, P., 2017. Preparation and characterization of magnetic and porous metal-ceramic nanocomposites from a zeolite precursor and their application for DNA separation. J. Biomed. Nanotechnol. 13, 337–348.
Pansini, M., Sannino, F., Marocco, A., Allia, P., Tiberto, P., Barrera, G., Polisi, M., Battista, E., Netti, P.A., Esposito, S., 2018. Novel process to prepare magnetic metal-ceramic nanocomposites from zeolite precursor and their use as adsorbent of agrochemicals from water. J. Environ. Chem. Eng. 6, 527–538.
Parise, J., Corbin, D., Abrams, L., Cox, D., 1984. Structure of dealuminated Linde Y-zeolite; Si139. 7Al52. 3O384 and Si173. 1Al18. 9O384: presence of non-framework Al species. Acta Crystallogr. Sect. C Cryst. Struct. Commun. 40, 1493–1497.
Pegis, M.L., Roberts, J.A., Wasylenko, D.J., Mader, E.A., Appel, A.M., Mayer, J.M., 2015. Standard reduction potentials for oxygen and carbon dioxide couples in acetonitrile and N, N-dimethylformamide. Inorg. Chem. 54, 11883–11888.
Quintanilla, A., Casas, J., Rodriguez, J., 2010. Hydrogen peroxide-promoted-CWAO of phenol with activated carbon. Appl. Catal. B Environ. 93, 339–345.
Ribeiro, A.R.L., Moreira, N.F., Puma, G.L., Silva, A.M., 2019. Impact of water matrix on the removal of micropollutants by advanced oxidation technologies. Chem. Eng. J. 363, 155–173.
Rouquerol, J., Llewellyn, P., Rouquerol, F., 2007. Is the BET equation applicable to microporous adsorbents. Stud. Surf. Sci. Catal. 160, 49–56.
Rueda Márquez, J.J., Levchuk, I., Sillanpää, M., 2018. Application of catalytic wet peroxide oxidation for industrial and urban wastewater treatment: a review. Catalysts 8, 673.
Sacco, O., Vaiano, V., Navarra, W., Daniel, C., Pragliola, S., Venditto, V., 2021. Catalytic system based on recyclable Fe0 and ZnS semiconductor for UV-promoted degradation of chlorinated organic compounds. Separ. Purif. Technol. 270, 118830.
Saeed, M., Ilyas, M., 2013. Oxidative removal of phenol from water catalyzed by nickel hydroxide. Appl. Catal. B Environ. 129, 247–254.
Sannino, D., Vaiano, V., Isupova, L.A., Ciambelli, P., 2011. Photo-Fenton oxidation of acetic acid on supported LaFeO3 and Pt/LaFeO3 perovskites. Chem. Eng. Trans 25, 1013–1018.
Sannino, D., Vaiano, V., Isupova, L.A., Ciambelli, P., 2012. Heterogeneous photo-Fenton oxidation of organic pollutants on structured catalysts. J. Adv. Oxid. Technol. 15, 294–300.
Sannino, F., Ruocco, S., Marocco, A., Esposito, S., Pansini, M., 2013. Simazine removal from waters by adsorption on porous silicas tailored by sol–gel technique. Microporous Mesoporous Mater. 180, 178–186.
Sannino, F., Pansini, M., Marocco, A., Cinquegrana, A., Esposito, S., Tammaro, O., Barrera, G., Tiberto, P., Allia, P., Pirozzi, D., 2022. Removal of sulfanilamide by tailor-made magnetic metal-ceramic nanocomposite adsorbents. J. Environ. Manag. 310, 114701.
Santos, B.L., Parpot, P., Soares, O.S., Pereira, M.F., Rombi, E., Fonseca, A.M., Correia Neves, I., 2020. Fenton-type bimetallic catalysts for degradation of dyes in aqueous solutions. Catalysts 11, 32.
Saragi, T., Depi, B., Butarbutar, S., Permana, B., 2018. The impact of synthesis temperature on magnetite nanoparticles size synthesized by co-precipitation method. In: Journal of Physics: Conference Series. IOP Publishing, 012190.
Schneider, J.T., Firak, D.S., Ribeiro, R.R., Peralta-Zamora, P., 2020. Use of scavenger agents in heterogeneous photocatalysis: truths, half-truths, and misinterpretations. Phys. Chem. Chem. Phys. 22, 15723–15733.
Schwarz, E.J., 1975. Magnetic Properties of Pyrrhotite and Their Use in Applied Geology and Geophysics.
Segneanu, A.E., Orbeci, C., Lazau, C., Sfirloaga, P., Vlazan, P., Bandas, C., Grozescu, I., 2013. Waste water treatment methods. Water Treat. 53–80.
Shafia, E., Esposito, S., Manzoli, M., Chiesa, M., Tiberto, P., Barrera, G., Menard, G., Allia, P., Freyria, F.S., Garrone, E., 2015. Al/Fe isomorphic substitution versus Fe 2 O 3 clusters formation in Fe-doped aluminosilicate nanotubes (imogolite). J. Nanoparticle Res. 17, 1–14.
Shi, B., Zhao, C., Ji, Y., Shi, J., Yang, H., 2020. Promotion effect of PANI on Fe-PANI/Zeolite as an active and recyclable Fenton-like catalyst under near-neutral condition. Appl. Surf. Sci. 508, 145298.
Shirvani, S., Ghashghaee, M., Kegnæs, S., 2019. Dual role of ferric chloride in modification of USY catalyst for enhanced olefin production from refinery fuel oil. Appl. Catal. Gen. 580, 131–139.
Singh, J., Kalamdhad, A., 2011. Effects of Heavy Metals on Soil. human, Plants.
Suarez-Ojeda, M.E., Carrera, J., Metcalfe, I.S., Font, J., 2008. Wet air oxidation (WAO) as a precursor to biological treatment of substituted phenols: refractory nature of the WAO intermediates. Chem. Eng. J. 144, 205–212.
Tahari, M.N.A., Salleh, F., Saharuddin, T.S.T., Dzakaria, N., Samsuri, A., Hisham, M.W. M., Yarmo, M.A., 2019. Influence of hydrogen and various carbon monoxide concentrations on reduction behavior of iron oxide at low temperature. Int. J. Hydrogen Energy 44, 20751–20759.
Tammaro, O., Barrera, G., Allia, P., Tiberto, P., Marocco, A., Manzoli, M., Bonelli, B., Confalonieri, G., Arletti, R., Pansini, M., 2023. Unravelling the role of the exchanged Ni amount in zeolites a and X for their thermal transformation into magnetic metal-ceramic nanocomposites. Ceram. Int.
Tiernan, M.J., Barnes, P.A., Parkes, G.M., 2001. Reduction of iron oxide catalysts: the investigation of kinetic parameters using rate perturbation and linear heating thermoanalytical techniques. J. Phys. Chem. B 105, 220–228.
Toby, B.H., 2001. EXPGUI, a graphical user interface for GSAS. J. Appl. Crystallogr. 34, 210–213.
U. EPA, 2002. Toxicological Review of Phenol. USA.
Vaiano, V., Isupova, L.A., Ciambelli, P., Sannino, D., 2014. Photo-fenton oxidation of t-butyl methyl ether in presence of LaFeO3 supported on monolithic structure. J. Adv. Oxid. Technol. 17, 187–192.
Vaiano, V., Iervolino, G., Sannino, D., Rizzo, L., Sarno, G., Ciambelli, P., Isupova, L., 2015. Food azo-dyes removal from water by heterogeneous photo-Fenton with LaFeO 3 supported on honeycomb corundum monoliths. J. Environ. Eng. 141, 04015038.
Vaiano, V., Matarangolo, M., Murcia, J., Rojas, H., Navío, J.A., Hidalgo, M., 2018. Enhanced photocatalytic removal of phenol from aqueous solutions using ZnO modified with Ag. Appl. Catal. B Environ. 225, 197–206.
Vaiano, V., Jaramillo-Paez, C.A., Matarangolo, M., Navío, J.A., del Carmen Hidalgo, M., 2019. UV and visible-light driven photocatalytic removal of caffeine using ZnO modified with different noble metals (Pt, Ag and Au). Mater. Res. Bull. 112, 251–260.
Verboekend, D., Vilé, G., Pérez-Ramírez, J., 2012. Hierarchical Y and USY zeolites designed by post-synthetic strategies. Adv. Funct. Mater. 22, 916–928.
Villegas, L.G.C., Mashhadi, N., Chen, M., Mukherjee, D., Taylor, K.E., Biswas, N., 2016. A short review of techniques for phenol removal from wastewater. Current Pollution Reports 2, 157–167.

Weidenthaler, C., Zibrowius, B., Schimanke, J., Mao, Y., Mienert, B., Bill, E., Schmidt, W., 2005. Oxidation behavior of ferrous cations during ion exchange into zeolites under atmospheric conditions. Microporous Mesoporous Mater. 84, 302–317.
Xing, W.D., Lee, M.S., Choi, S.H., 2018. Separation of Ag (I) by ion exchange and cementation from a raffinate containing Ag (I), Ni (II) and Zn (II) and traces of Cu (II) and Sn (II). Processes 6, 112.
Zhang, Y., Zhou, M., 2019. A critical review of the application of chelating agents to enable Fenton and Fenton-like reactions at high pH values. J. Hazard Mater. 362, 436–450.
Zhang, J., Tang, X., Yi, H., Yu, Q., Zhang, Y., Wei, J., Yuan, Y., 2022. Synthesis, characterization and application of Fe-zeolite: a review. Appl. Catal. Gen. 630, 118467.
Zhong, J., Yang, B., Feng, Y., Chen, Y., Wang, L.-G., You, W.-D., Ying, G.-G., 2021. Enhanced photo–fenton removal efficiency with core-shell magnetic resin catalyst for textile dyeing wastewater treatment. Water 13, 968.
Zieliński, J., Zglinicka, I., Znak, L., Kaszkur, Z., 2010. Reduction of Fe2O3 with hydrogen. Appl. Catal. Gen. 381, 191–196.